

Reverse-Shock in Tycho's Supernova Remnant

F.J. Lu¹, M. Y. Ge¹, S. J. Zheng¹, S. N. Zhang¹, X. Long¹, and B. Aschenbach²

¹*Key Laboratory for Particle Astrophysics, Institute of High Energy Physics, Chinese Academy of Sciences, Beijing 100049, P.R. China; lufj@ihep.ac.cn; gemy@ihep.ac.cn*

²*PR Vaterstetten, Mozartstraße 8, 85591 Vaterstetten, Germany*

ABSTRACT

Thermal X-ray emission from young supernova remnants (SNRs) is usually dominated by the emission lines of the supernova (SN) ejecta, which are widely believed being crossed and thus heated by the inwards propagating reverse shock (RS). Previous works using imaging X-ray data have shown that the ejecta are heated by the RS by locating the peak emission region of the most recently ionized matter, which is found well separated towards the inside from the outermost boundary. Here we report the discovery of a systematic increase of the Sulfur (S) to Silicon (Si) $K\alpha$ line flux ratio with radius in Tycho's SNR. This allows us, for the first time, to present continuous radial profiles of the ionization age and, furthermore, the elapsed ionization time since the onset of the ionization, which tells the propagation history of the ionization front into the SNR ejecta.

Subject headings: ISM: supernova remnants—supernovae: general—supernovae: individual (Tycho's SN)

1. Introduction

The reverse shock (RS) plays a key role in the study of explosive phenomena such as supernova (SNe) and gamma-ray bursts (GRBs). When a SN explodes, a blast wave (BW) is generated and propagates into the ambient medium, with fast moving ejecta following behind. In the 1970s, it was proposed that an inward-propagating shock wave, the so-called RS, will accompany the deceleration of the ejecta by the ambient medium, and the ejecta behind this shock can be a strong source of thermal X-rays (Gull 1973; Rosenberg & Scheuer 1973; McKee 1974; Gull 1975). As the ejecta expand, their density and pressure decrease,

which causes the RS to accelerate (McKee 1974), and simulations show that in supernova remnants (SNRs) the velocity of the RS could be eventually much higher than that of the BW (Truelove & McKee 1999), resulting in a hot core enclosed by a cooler shell (Vink 2012). The X-ray emission from the RS-heated ejecta thus provides important information about the chemical evolution of stars and galaxies. In GRB study, the RS is used to explain the early time flares and emission excess in the optical and radio bands and is regarded as the most useful probe of the initial bulk Lorentz factor and the ejecta composition (Mészáros & Rees 1993; Mészáros 2002; Sari & Piran 1999; Kobayashi & Zhang 2003; Laskar et al. 2013). The RS propagating back into the accretion flow from the normal companion star is also suggested to be the cause of a weak Hydrogen emission line that varies in radial velocity in a cataclysmic variable system (Krauland et al. 2013). Therefore, the RS is important for a wide range of astrophysics study.

The best sites to study the dynamics of the RS are SNRs because of their fairly large angular sizes. Observations and analyses of the X-ray emission from a few young SNRs have established the action of RS, as the X-ray emission properties of plasma are related to its shock heating history. After matter is crossed and heated by a shock, the atoms start to be ionized gradually, and the ionization age ($\tau = n_e t$, where n_e is the electron number density and t the time span since the shock heating) is used in SNR study to describe the ionization state of plasma (Itoh 1977). Since the line emission properties of the ejecta in a SNR change with τ , spatial variation of those properties could be used to trace the propagation of the shock that heats the ejecta. In the RS scenario, the ejecta in the outer layers should generally have a higher τ than in the inner layers, and evolution of line emission properties with radius is thus expected. Most of the evidence for RS is obtained by this method so far.

X-ray imaging spectroscopy of the Tycho’s SNR by Hwang and Gotthelf (1997) using the *ASCA* data showed that for the Tycho’s SNR the Fe $K\alpha$ line emission has its peak at a smaller radius than the Fe-L and Si-K emission. Based on a detailed broad band X-ray spectral analysis of the *ASCA* data Hwang et al. (1998) determined a significantly lower τ for the Fe-K band emission than for the Fe-L and Si-K emission bands, which they attributed to a more recent heating of the Fe-K line emitting ejecta by the RS. Warren et al. (2005) used the so-called Principal Component Analysis technique to study images and spectra taken with the Chandra X-ray Observatory (hereafter *Chandra*) to disentangle between emission regions which are either line-dominated or featureless-dominated. On the basis of the obtained morphology the authors determined the locations of the BW, the contact discontinuity and the inner edge of the RS, such that $r = 0.7$ with r the ratio of the radii of the RS over that of the BW. They also suggest that the Fe-K band emission comes from the innermost portion of the shocked ejecta and its inner edge denotes the location of the RS. These interpretations would require some stratification of the elements throughout

the explosion and subsequently, at least as far as the bulk of the Fe emission is concerned, which has to remain inside of the region populated by the intermediate-mass elements like Si and S. To be consistent with the high temperatures required for the Fe-K band emission observed by Hwang and Gotthelf (1997), an additional heating process of the electrons in the area of the RS is needed, e.g., collisionless electron heating, as proposed by Badenes et al. (2005). One-dimensional delayed detonation models for the SN coupled with non-equilibrium ionization of the shock heated ambient plasma and the RS heated ejecta were compared with the images and spatially integrated spectra of this remnant obtained with *Chandra* and *XMM-Newton*, which could be well reproduced with some degree of chemical stratification of the ejecta and the Fe-K emission peaking interior to the intermediate-mass element distribution (Badenes et al. 2006).

Application of the same kind of approach leads to a satisfactory agreement with the observations of SNR 0509-67.5 located in the Large Magellanic Cloud (Badenes et al. 2008). Similarly, the *Chandra* X-ray observations of Kepler’s SNR could be explained with hydrodynamical modeling by Patnaude et al. 2012. For SN1006 the *Suzaku* measurements are consistent with chemical stratification but based on the spatially integrated X-ray spectra the RS may not have reached or heated the supposedly interior Fe shell (Yamaguchi et al. 2008). The topic of chemical stratification of the elements in young SNR, which is highly relevant to the supposedly innermost Fe-K band emission and therefore to possibly the innermost edge of the RS is further addressed by Yamaguchi et al. (2014a) for Tycho’s SNR, and Yamaguchi et al. (2014b), more generally, for young and middle-aged SNRs with Fe $K\alpha$ emission. Yamaguchi et al. (2014a) report the detection of Fe $K\beta$ fluorescence emission from low ionization Fe at a radius even smaller than the peak radius of the Fe α line emission at $r = 0.66$.

In addition to the above facts obtained from the line emission properties, there are some other evidence supporting the RS scenario. In Cassiopeia A, a sharp rise of the radio and Si emissivity at the inner edge of the bright X-ray ring was suggested to be associated with the RS (Hwang et al. 2000). It has also been shown that the available multi-wavelength observations in the radio, X-ray, and gamma-ray bands of Cassiopeia A can be best explained by invoking particle acceleration by both forward and RSs (Zirakashvili et al. 2014). In SN1987 A, the broad Ly α emission feature located inside the inner ring was attributed to the excitation by a RS (Sonneborn et al. 1998; Michael et al. 2003), which would indicate the position of the RS front. Hubble Space Telescope observations of a star located behind the SN 1006 remnant revealed that the ejecta had been decelerated probably by the RS by $44 \pm 11 \text{ km s}^{-1}$ from year 1999 to 2010 (Winkler et al. 2011).

Summarizing the previous works, the observations and subsequent analyses have allowed

to locate the bulk or peaks of the emission of the most recently shocked matter, by which the existence of the RS in these SNRs has been demonstrated. In this paper we would like to go one step further, i.e., outlining the evolution of the RS by measuring the radial profile of the ionization age from the outer edge of the ejecta, or the so called contact discontinuity, as far as possible towards the center of Tycho’s SNR by using the data from the archived long exposure observations made in 2009 with *Chandra*. Tycho’s SNR is relatively nearby (~ 3 kpc) (de Vaucouleurs 1985; Hernández et al. 2009), bright in X-rays, and has a quite symmetric morphology (Lu et al. 2011), which means that the shock structure should be regular and thus easy to be revealed, and it is indeed the most widely studied SNR as to the existence of RS. We also attempt to separate electron density and the time since the onset of the RS shock heating at a given radius, i.e., a time profile for the ionization. In this way the progression of the RS towards the interior of the SNR is documented rather than determining just the location of its inner edge.

Instead of doing X-ray spectral modeling to get the τ of the plasma in different regions, here we have searched for signals of the RS kinematics by using the relative strength of the silicon (Si) and sulfur (S) $K\alpha$ emission lines across the Tycho’s SNR. With the high spatial and spectral resolution X-ray observations of young SNRs available, one may think that it is possible to obtain τ of the plasma in a region by modelling its X-ray spectrum, and the RS behavior could be revealed with such analyses for a series of spectra taken at different radii. However, it is very difficult in practice, because the plasma along the line of sight usually contains many clumps that have quite different abundances, temperatures, densities and ionization states. In contrast, using the relative strength of the Si and S lines is more robust and straight forward. In various SN models, Si and S are synthesized in similar physical conditions and are therefore expected to be well mixed spatially, or with S locating only very slightly inside Si, at most (Nomoto 1997; Iwamoto et al. 1999; Höflich et al. 2002; Höflich et al. 2006). This is also confirmed observationally for Tycho’s SNR by the similar overall temperature and τ of these two elements (Hwang et al. 1998). Therefore, Si and S should be very similar in temperature, density, and τ distributions, and the comparison of their line emission strengths could be used to trace the propagation of the RS.

2. Observation and Results

The data we analysed were obtained in 2009 with the imaging array of the Advanced CCD Imaging Spectrometer (ACIS-I) aboard *Chandra* for a total effective exposure of 734 ks. The observations are listed in Table 1. The data were calibrated with Chandra Interactive

Analysis of Observations (CIAO V4.5) following the standard procedure¹. Throughout this paper the uncertainties are at 1σ level.

2.1. X-ray Images

Fig. 1 presents the X-ray maps of the remnant in 0.5-8.0, 1.6-2.0, and 2.2-2.6 keV energy bands, as well as its 2.2-2.6 keV to 1.6-2.0 keV intensity ratio map. Intensities in 2.2-2.6 keV and 1.6-2.0 keV are dominated by the Helium-like (He-like) S and Si $K\alpha$ lines, respectively. Therefore, Fig. 1(d) clearly shows that the S/Si line intensity ratio in an outer shell is higher than that in the inner part.

2.2. Radial distributions of the Si and S line fluxes and their ratio

To study the variations of the line flux ratio at different radii in a more quantitative way, spectra of three series of annuli have been extracted and fitted to get the fluxes of the Si $K\alpha$ (~ 1.86 keV) and S $K\alpha$ (~ 2.45 keV) lines. Regions from which the annulus series were extracted are denoted in Fig. 1. The width of the annuli is $4''$ in the outer regions, increases to $8''$ in the inner regions, and becomes even wider in the inmost fans, so as to have enough photons for each spectrum. The background spectrum was extracted from regions outside of the remnant, and the spectra were analyzed with XSPEC (v12.7.1). The spectrum of an annulus was fitted with a two-component VNEI model (Borkowski et al. 2001) that describes the X-ray emission spectrum of plasma in non-equilibrium ionization state, with the temperatures, emission measures, ionization age τ , abundances of the elements as free parameters and the redshift fixed at zero. The WABS model (Morrison & McCammon 1983) with the column density fixed at $6 \times 10^{21} \text{ cm}^{-2}$ was used to account for the interstellar medium absorption, and a Gaussian line at 3.1 keV was added to represent the Ar emission lines, which is missing in the VNEI model. The absorption column density used here is similar to that of Warren et al. (2005), and to set it at $5 \times 10^{21} \text{ cm}^{-2}$ or $7 \times 10^{21} \text{ cm}^{-2}$ does not change our main results significantly.

Now we describe the process to get the fluxes of the lines. For Si, we first fitted the spectrum with a two-component VNEI model, then set the Si abundance to zero, and used four Gaussian components to account for the emission from Si. In the four Gaussian components, one with the central energy at about 1.85 keV corresponds to the prominent $K\alpha$ line,

¹<http://cxc.harvard.edu/ciao>

the other three with central energies fixed at 2.006, 2.182 and 2.294 keV and width fixed as 10^{-5} keV represent the Ly α , the He β , and the He γ lines, respectively. The He γ flux was set as 0.55 He β flux in the fitting process, which is typical for a plasma around 1 keV as in this remnant (e.g., Hwang & Gotthelf 1997). The flux of the Gaussian component at ~ 1.85 keV is used in our S/Si line flux ratio study. For S, the analysis process is the same. The flux of the first component at about 2.45 keV represents the He K α line and is used for the S/Si line flux ratio study, while the other three components with central energies fixed at 2.623, 2.884 and 3.033 keV and width fixed as 10^{-5} keV represent the Ly α , the He β and the He γ lines of S, respectively. The S He γ flux was set as 0.56 He β flux, also following Hwang & Gotthelf (1997). Fig. 2 illustrates an example of the spectral fitting results, and Table 2 lists the fitted parameters of the corresponding Gaussian components. The S to Si line flux ratios versus distances from the geometrical center (Warren et al. 2005) for these regions are plotted in Fig. 3. Apparently, the ratio increases with radius for every of the three regions, except of some small bumps caused by bright fragments in projection.

The errors of the line fluxes plotted in Fig. 2 and those listed in Table 2 are obtained in the spectral fitting process by using the *error* command in XSPEC. In this process the continuum emission was fixed, and so the line flux uncertainty induced by the continuum determination had not been included. We thus used a Monte-Carlo method to estimate how significant this fraction of error is. For the spectrum shown in Fig 2, as an example, we sampled it 500 times and got 500 simulated spectra. Then we repeated the spectral fitting and Gaussian fitting processes and got 500 pairs of Si and S K α line flux values. The distributions of the Si and S line fluxes as well as their ratios are presented in Fig 4, whose widths could be taken as the statistical errors of these quantities. Fitting the distributions with a Gaussian function gives the 1σ values of 1.5% and 3.7% for the Si and S lines, respectively, quite similar to those listed in Table 2, which are 1.4% and 3.2%. Therefore the contribution of the continuum determination to the line flux uncertainty could be neglected, and the line flux uncertainties used in this paper are thus directly derived by the *error* command of XSPEC.

3. Discussion

The observed radial distributions of the S/Si line flux ratios provide an opportunity to study the shock heating history of the plasma. As introduced earlier, S distributes very similarly to or at most a little closer to the inside than Si, the S/Si abundance ratio should be almost constant or slightly decrease with radius (e.g., Nomoto 1997; Iwamoto et al. 1999; Höflich et al. 2002; Höflich et al. 2006). The observed S/Si line flux ratios that increase

with radius are thus not the results of abundance changes, but the variation of τ and/or temperature of the plasma versus radius, which will be discussed below.

In Fig. 5, the S/Si flux ratios as a function of τ (predicted by the VNEI model) are plotted for various electron temperatures, where the S/Si abundance ratio is assumed to be 1.35 times the solar value (Hwang & Gotthelf 1997). Apparently, a high S/Si K α line flux ratio corresponds to a higher temperature and/or τ , and thus the observed S to Si line flux ratio profiles plotted in Fig. 3 are the consequence of increasing temperature and/or τ with radius. However, previous observations of the Tycho’s SNR found that the temperature is actually higher in the interior (Decourchelle et al. 2001; Warren et al. 2005), which is also supported by numerical simulations (Badenes et al. 2006). Thus the only explanation of Fig. 3 is that τ increases with radius.

In order to further find out which of n_e and t dominates the observed τ variations, we deprojected the observed radial profiles of Si, S, and thermal continuum fluxes to obtain the S/Si line flux ratios and the scaled emission measure in real space. The observed surface flux $F(r)$ in a direction is the integration of the volume flux $F_d(r)$ along the line of sight. Under the assumption of spherical symmetry the formula is (Helder & Vink 2008):

$$F(r) = \int_r^R F_d(r') \frac{r'}{\sqrt{r'^2 - r^2}} dr' \quad (1)$$

where R is the outermost radius of the object. The deprojection was performed from the outermost to the inner regions by using this formula. In the deprojection process, the deprojected volume flux $F_d(r)$ is very sensitive to the fluctuations of the observed surface flux $F(r)$. We therefore smoothed the $F(r)$ profile with a Gaussian function of $FWHM = 0.0235$ (or 1σ width of 0.01, with the outermost radius scaled to 1), and then deprojected the smoothed one. The inner boundary of the X-ray emitting ejecta shell was set to the position where $F_d(r)$ first touches zero. Fig. 6 shows the comparison between the observed radial profiles ($F(r)$) and those ($F_p(r)$) reprojected from $F_d(r)$, while Fig. 7 shows the deprojected ones. As shown, $F_p(r)$ fits the observed surface brightness $F(r)$ fairly well, especially in regions with $r > 0.75$. However, in the inner regions there exist some deviations. These deviations imply that $F(r)$ is not the projection of a perfectly spherical emission distribution. Especially it is relatively deficient of emission in the central region. Therefore, the deprojected flux profiles are qualitatively reliable but may not be correct quantitatively.

The errors of $F_d(r)$ were also obtained with a Monte-Carlo method. For each distribution, using $F(r)$ as the expected value and its error obtained in the spectral fitting as the 1σ width of the Gaussian distribution, we simulated 100 surface flux distribution curves, from which 100 deprojected volume flux curves have been derived. Fig. 8 plots the distribution of these 100 simulated volume fluxes at each radius. The uncertainty of the deprojected

volume flux $F_d(r)$ plotted in Fig. 7 is actually the 1σ width of the distribution, similar to the procedure shown in Fig. 4.

The continuum emission profiles in Figs. 6 (the 3rd row) and 7 are inferred from the 0.85-1.5 keV plus 3.0-10.0 keV fluxes with the nonthermal contribution subtracted. We select these two energy bands so as to eliminate the influence of the strong Si and S emission lines. The flux of the nonthermal emission is extrapolated by using the 4.0-6.0 keV flux, because the 4.0-6.0 keV emission is dominated by the nonthermal emission (e.g., Warren et al. 2005; Eriksen et al. 2011; Lu et al. 2011). In the flux extrapolation, the photon indices are not the same for all the spectra. For those in regions 1 and 3 we use the photon index of the nonthermal emission of the entire remnant, which is 2.7 (e.g., Warren et al. 2005; Tamagawa et al. 2009). However, the spectral photon indices for the nonthermal components in region 2 are slightly different. Eriksen et al. (2011) found that the nonthermal strips in that region have harder spectra than the nonthermal spectrum of the entire remnant, the brightest strip has an index of ~ 2.1 , and the other weaker strips have a mean index of ~ 2.5 . Therefore, when we calculate the nonthermal fluxes for the annuli in region 2, their photon indices are actually the mean of those for the diffuse emission, the weak strips, and the brightest strip weighted by their respective 4.0-6.0 keV photon counts in each annulus, and the resulted photon indices are in the range of 2.63-2.7. The 3rd to 5th rows of Fig. 6 plot the thermal continuum emission, nonthermal emission, and the nonthermal to thermal ratio profiles.

Now we estimate the uncertainties of the thermal emission flux that introduced by the subtraction of the nonthermal component, which is in turn related to the errors of the nonthermal flux. One error source of the nonthermal flux is the contamination of the thermal emission. This contamination will result in over-estimation of the nonthermal flux and then under-estimation of the thermal flux. As shown in the bottom panel of Fig. 6, except for the rims of the remnant, the nonthermal emission is only about 5-20% as strong as the thermal emission. Considering that the thermal contribution to the 4.0-6.0 keV energy flux is $\sim 10\%$ at the rims and increase to $\sim 40\%$ in the inner regions (Warren et al. 2005; Eriksen et al. 2011), we realise that the thermal continuum flux could be over-subtracted up to $\sim 8\%$. The other error source of the nonthermal emission is the variation of the photon indices. As discussed above, the lowest photon index of the spectra in region 2 could be 2.63 due to the existence of the harder nonthermal strips, which implies that the photon indices used in this paper might deviate from the actual ones up to 0.07. Simple calculations show that, if the 4.0-6.0 keV flux (in units of $\text{erg cm}^{-2} \text{s}^{-1}$) is the same, the 0.85-1.5 plus 3.0-10.0 keV flux of a spectrum with photon index of 2.63 is about 2.8% lower than that of a spectrum with photon index of 2.7. This flux difference can be considered as the typical error of the nonthermal fluxes caused by the variation of photon indices. As the 0.85-1.5 plus 3.0-10.0 keV thermal emission flux dominates the nonthermal flux except at the rims ($r \geq 0.95$),

we conclude that the photon index variations of the nonthermal emission have negligible influence on the determination of the thermal fluxes. In summary, the typical errors of the thermal continuum fluxes introduced by the subtraction of the nonthermal component is less than $\sim 8\%$, much smaller than the overall variations of the radial profiles.

The scaled electron density n_e plotted in the 4th row of Fig. 4 is simply the square root of the emission measure represented by the deprojected thermal continuum fluxes (the 3rd row of Fig. 7). Actually, the emission measure is proportional to $n_e * n_H$, which is $1.18 n_H^2$ (or $0.85 n_e^2$) for plasma of solar abundance, and n_e is proportional to the square root of the thermal continuum fluxes with an accuracy of $(1.18^{1/2} - 1) = 9\%$. Decourchelle et al. (2001) studied the spectra of several typical regions in the Tycho’s SNR. They found that in the knot where the heavy element is most abundant, the Si abundance is 4.2 times of solar value, S is 6.9, and Fe is 0.7. It is thus reasonable to set the upper limit of the heavy element abundance as 7 times solar values. If all these elements are fully ionized, n_e is $1.24n_H$, or the emission measure is proportional to $0.80 n_e^2$. In this case, n_e is proportional to the square root of the thermal continuum fluxes with an accuracy better than $(1.24^{1/2} - 1) = 11\%$. We also note that Hwang et al. (1998) obtained a much higher abundance of about 30 times solar value for heavy elements such as Si and S. Even if all the elements are that abundant and fully ionized, n_e will be $1.48n_H$, and n_e will be proportional to the square root of the thermal continuum fluxes with an accuracy about $(1.48^{1/2} - 1) = 22\%$. Based on these discussions we concluded that the elemental abundance variation in the ejecta can not change much the radial profiles of n_e shown in the 4th row of Fig. 7.

As can be seen in Fig. 7, the S/Si line ratios increase almost monotonically with r , while n_e have big bumps at r between 0.9 and 0.75, which means that t must increase with radius and dominate the τ variations. So the ejecta in the outer region were heated earlier. This is just what the RS scenario means. For reference, we inferred from the S/Si line ratio the τ values under the assumption that the temperature is constant (1.0 keV) and the S/Si abundance ratio is 1.35 solar value (Hwang & Gotthelf 1997). As plotted in the bottom panel of Fig. 7, the decrease of τ to the remnant center is quite obvious.

For the sake of the argument, we outline the consequences for the case that the plasma emitting the bulk of the Si and S lines were heated by a forward shock. The pre-shock medium were required to be enriched in Si and S and should have a density that increases with radius. Such a profile is very unlikely to exist, neither for the ejecta shortly after the SN explosion nor for a putative ambient interstellar medium. The stellar matter ejected a long time before the explosion could have such a density distribution. But there is no observational evidence at any other wavelength for the existence of such a shell or ring, strongly supporting our findings that t increases with radius.

4. Summary

Using the long exposure *Chandra* ACIS-I observations of Tycho’s SNR, we have obtained radial distributions of the He-like $K\alpha$ lines of Si and S for three fan-like regions where the brightness distributions look spherically symmetric. In all the three regions, both the observed and the deprojected S/Si line flux ratios increase almost monotonically with distance from the remnant center. We have shown that this line flux ratio is a good tool to investigate the shock wave kinematics in young SNRs, and the observed results can only be explained if the ejecta in the outer regions were heated earlier. Therefore, we provide for the first time radial profiles of the RS action in Tycho’s SNR, equivalent to the temporal evolution of the RS. Furthermore, our study may also provide a potential new method to derive the time development of the RS velocity giving additional insight to the hydrodynamic processes in young SNRs by eventually more detailed studies of radial variations of the S/Si line flux ratios as well as the plasma temperatures and densities.

Acknowledgments

F.J.L and M.Y.G contributes equally to this work. We thank Q.Daniel Wang, Yang Chen, Aigen Li and Mei Wu for very useful suggestions. F.J.L thanks Kenichi Nomoto for helpful discussions. This work is supported by grants from National Science Foundation of China (11233001,11133002).

REFERENCES

- Badenes, C., Borkowski, Bravo, E. 2005, ApJ, 624, 198
- Badenes, C., Borkowski, K. J., Hughes, J.P., Hwang, U., Bravo, E. 2006, ApJ, 645, 1373
- Badenes, C., Hughes, J.P., Bravo, E., Langer, N. 2007, ApJ, 662, 472
- Badenes, C., Hughes, J.P., Hwang, U., Cassam-Chenaï, G., Bravo, E. 2008, ApJ, 680, 1149
- Borkowski, K. J., Lyerly, W.J., Reynolds, S. P. 2001, ApJ, 548, 820
- Decourchelle, A., Sauvageot, J. L., Audard, M., Aschenbach, B., Sembay, S., Rothenflug, R., Ballet, J., Stadlbauer, T., West, R. G. 2001, A&A, 365, L218
- de Vaucouleurs, G. 1985, ApJ, 289, 5
- Eriksen, K. A., et al. 2011, ApJ, 728, L28
- Gull, S. F. 1973, MNRAS, 161, 47
- Gull, S. F. 1975, ApJ, 171, 263
- Helder, E. A., Vink, J. 2008, ApJ, 686, 1094
- Hernández, J.I., et al. 2009, ApJ, 691, 1
- Höflich, P., Gerardy, C. L., Fesen, Robert A., Sakai, S., 2002, ApJ, 568, 791
- Höflich, P. 2006, Nuclear Physics A, 777, 579
- Hwang, U., Gotthelf, E. V. C. 1997, ApJ, 475, 665
- Hwang, U., Hughes, J.P., Petre, R. 1998, ApJ, 497, 833
- Hwang, U. H., Stephen S., Petre, Robert, 2000, ApJ, 537, 119
- Itoh, H., 1977, PASJ, 29, 813
- Iwamoto, K., Brachwitz, F., Nomoto, K., Kishimoto, N., Umeda, H., Hix, W. R., Thielemann, F.-K., 1999, ApJS, 125, 439
- Kobayashi, S., Zhang, B. 2003, ApJ, 582, 75
- Krauland, C. M., Drake, R. P., Kuranz, C. C., Louprias, B., Plewa, T., Huntington, C. M., Kaczala, D. N., Klein, S., Sweeney, R., Young, R. P., 2013, ApJ, 762, 2

- Laskar, T., Berger, E., Zauderer, B. A., Margutti, R., Soderberg, A. M., Chakraborti, S., Lunnan, R., Chornock, R., Chandra, P., Ray, A. 2013, *ApJ*, 776, 119
- Lu, F. J., Wang, Q. D., Ge, M. Y., Qu, J. L., Yang, X. J., Zheng, S. J., Chen, Y., 2011, *ApJ*, 732, 11
- McKee, C. F. 1974, *ApJ*, 188, 335
- Meszaros, P., Rees, M. J. 1993, *ApJ*, 418, 59
- Meszaros, P. 2002, *A&A*, 40, 137
- Michael, E., McCray, R., Chevalier, R., Filippenko, A. V., Lundqvist, P., Challis, P., Sugerman, B., Lawrence, S., Pun, C. S. J., Garnavich, P., 2003, *ApJ*, 593, 809
- Morrison, R., McCammon, D. 1983, *ApJ*, 270, 119
- Nomoto, K., Iwamoto, K., Nakasato, N., Thielemann, F.-K., Brachwitz, F., Tsujimoto, T., Kubo, Y., Kishimoto, N., 1997, *Nuclear Physics A*, 621, 467
- Patnaude, D. J., Badenes, C., Park, W., Laming, J. M. 2012, *ApJ*, 756, 6
- Sari, R., Piran, T. 1999, *ARA&A*, 520, 641
- Sonneborn, G., Pun, C. S. J., Kimble, R. A., Gull, T. R., Lundqvist, P., McCray, R., Plait, P., Boggess, A., Bowers, C. W., Danks, A. C., et al. 1998, *ApJ*, 492, 139
- Rosenberg, I., Scheuer P. A. G. 1973, *MNRAS*, 161, 27
- Ruiz-Lapuente, P., Comeron, F., Mndez, J., Canal, R., Smartt, S. J., Filippenko, A. V., Kurucz, R. L., Chornock, R., Foley, R. J., Stanishev, V., Ibata, R., 2004, *nature*, 431, 1069
- Tamagawa, T., et al. 2009, *PASJ*, 61, S167
- Truelove, J. K., Mckee, C. F. 1999, *ApJS*, 120, 299
- Vink, J. 2012, *ARA&A*, 20, 49
- Warren, J. S., Hughes, J. P., Badenes, C., Ghavamian, P., McKee, C. F., Moffett, D., Plucinsky, P. P., Rakowski, C., Reynoso, E., Slane, P. 2005, *ApJ*, 634, 376
- Winkler, P. Frank, Hamilton, A. J. S.; Long, K. S., Fesen, R. A. 2011, *ApJ*, 742, 80

Yamaguchi, H., Koyama, K., Katsuda, S., Nakajima, H., Hughes, J. P., Hiraga, J. S., Mori, K., Ozaki, M., Tsuru, T. G. 2008, PASJ, 60, S141

Yamaguchi, H., Eriksen, Kristoffer A., Badenes, C., Hughes, J. P., Brickhouse, N. S., Foster, A. R., Patnaude, D. J., Petre, R., Slane, P. O., Smith, R. K. 2014a, ApJ, 780, 136

Yamaguchi, H., Badenes, C., Petre, R., Nakano, T., Castro, D., Enoto, T., Hiraga, J.S., Hughes, J. P., Maeda, Y., Nobukawa, M., Safi-Harb, S., Slane, P.O., Smith, R.K., Uchida, H. 2014b, ApJ, 785, L25

Zirakashvili, V. N., Aharonian, F. A., Yang, R., Ona-Wilhelmi, E., Tuffs, R. J., 2014, ApJ, 785, 130

Table 1. Chandra ACIS-I observations of Tycho’s SNR in 2009.

ObsID	Start Date	Exposure(ks)
10093	2009-04-13	118
10094	2009-04-18	90
10095	2009-04-23	173
10096	2009-04-27	106
10097	2009-04-11	107
10902	2009-04-15	40
10903	2009-04-17	24
10904	2009-04-13	35
10906	2009-05-03	41
Total		734.11

Table 2. The fitted parameters of the 8 Gaussian components representing the Si and S line emission.

Elements	Components	Central Energy(keV)	Width(keV)	Flux(10^{-15} ergs cm^{-2} s^{-1})
Si	G1	1.853 (1.852, 1.854)	0.028 (0.026, 0.030)	10.29 (10.06, 10.43)
	G2	2.006*	1E-5*	0.83(0.74, 0.92)
	G3	2.182	1E-5	1.11 (1.05, 1.16)
	G4	2.294	1E-5	0.61 (0.58, 0.64)
S	G1	2.451 (2.448, 2.454)	0.019 (0.003, 0.027)	3.16 (3.06, 3.27)
	G2	2.623	1E-5	0.12 (0.05, 0.18)
	G3	2.884	1E-5	0.22 (0.20, 0.25)
	G4	3.033	1E-5	0.12 (0.11, 0.14)

*no error range given means that the parameter is fixed.

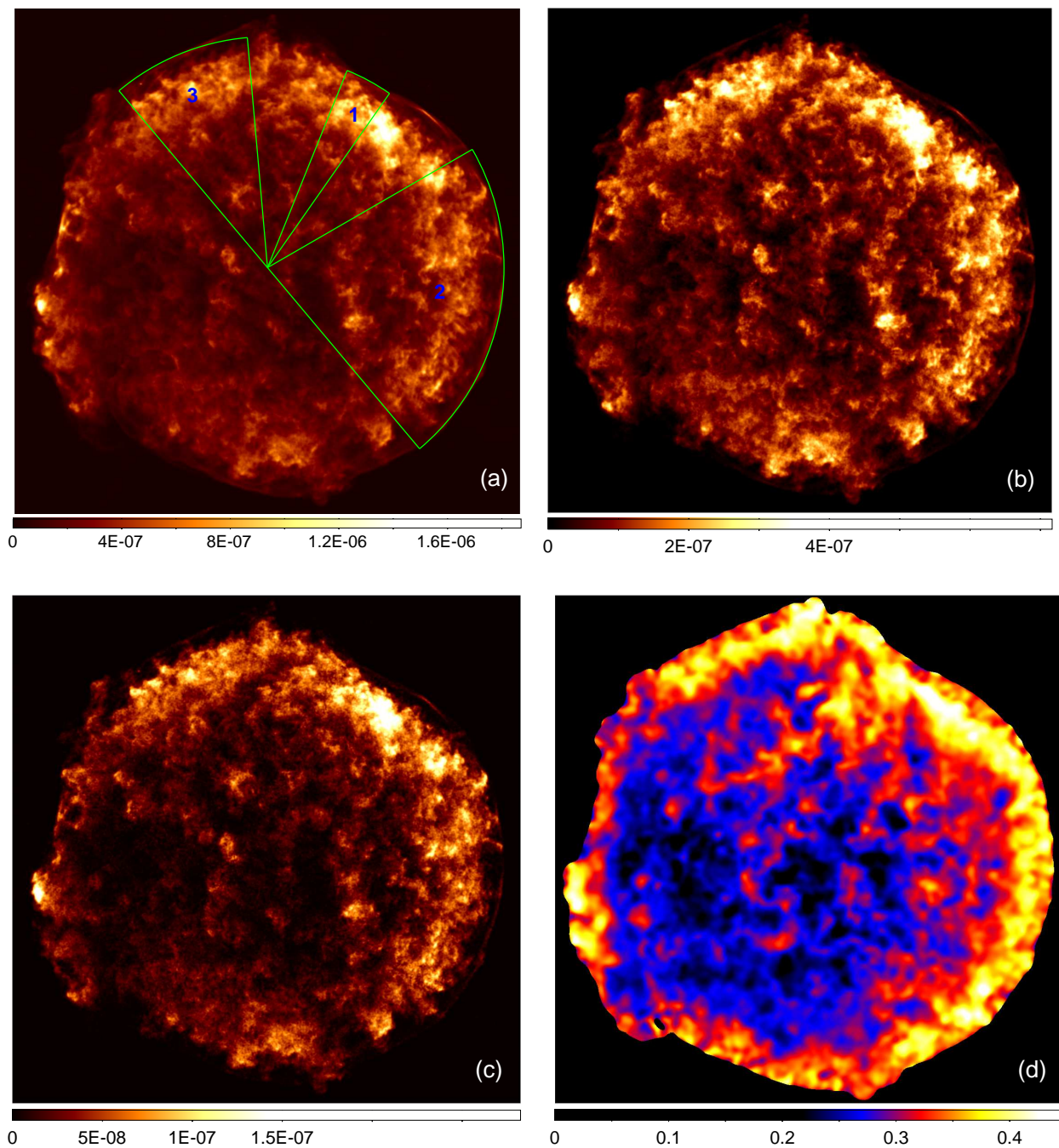


Fig. 1.— The X-ray intensity maps for the Tycho’s SNR in 0.5-8.0 keV(a), 1.6-2.0 keV(b) and 2.2-2.6 keV(c), as well as the 2.2-2.6 to 1.6-2.0 keV intensity ratio map (d) for this remnant. The images are obtained with *Chandra*/ACIS-I, and the intensities are in units of $\text{cts arcsec}^{-2} \text{s}^{-1}$. (b) is dominated by Si $K\alpha$ line, and (c) by the S $K\alpha$ line. (d) has been Gaussian-smoothed with the FWHM of $10''$, and the ratio of low brightness region outside the remnant has been set as zero. The three fan-like regions in (a) denote those for which spectral analyses have been performed.

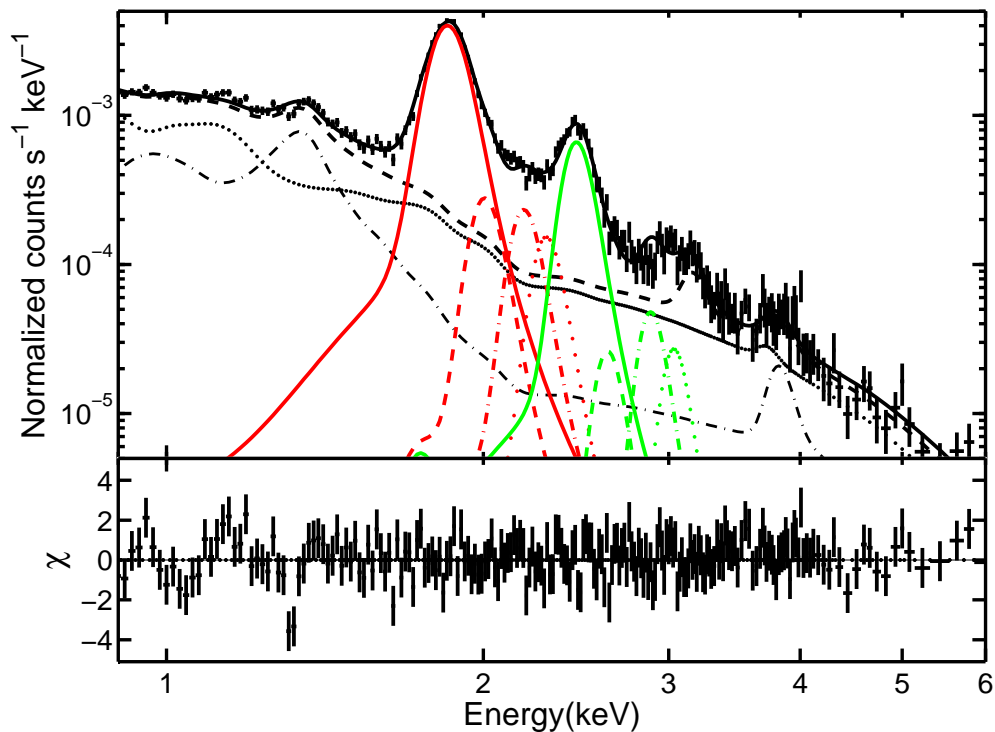


Fig. 2.— The X-ray spectrum of an annulus in region 3 with radius of $0''$ to $24''$. Upper panel: The solid black line represents the two-component VNEI model fitted to the data, and the dashed black line represents the same model but setting the Si and S abundances to zero. The red lines are the four components used to account for the Si line emission, while the four green lines are for S. The dotted and dash-dotted black lines are the two VNEI components respectively with the Si and S abundances fixed at zero. Lower panel: the residual of the (2 VNEI + 8 Gaussian) model fit to the data. The Si and S abundances in the 2 VNEI model have been set to zero as mentioned above.

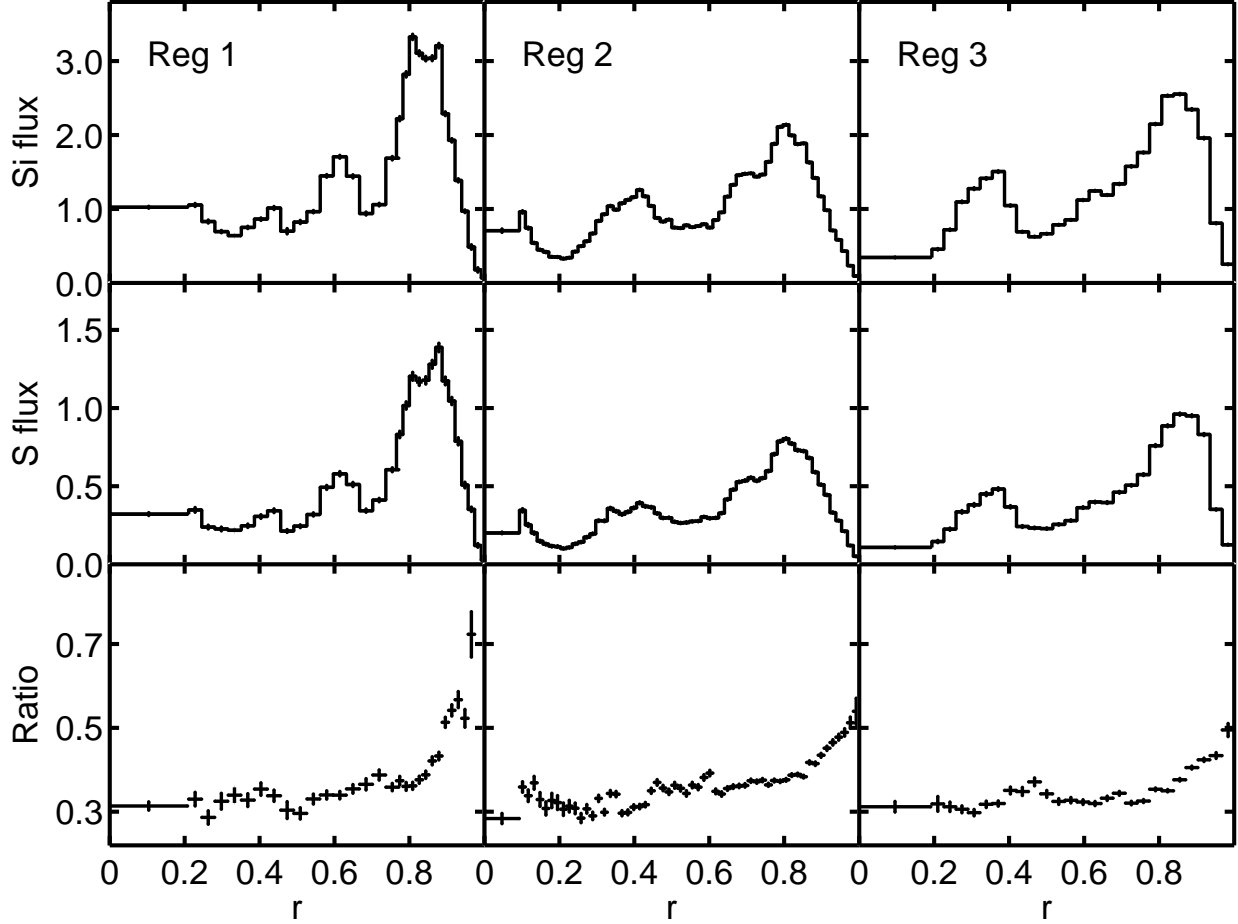


Fig. 3.— The Si and S He-like $K\alpha$ line flux properties as a function of radius (r) from the remnant center (RA(2000)= $00^h 25^m 19.4^s$, DEC(2000)= $64 08' 13.98''$) for the three regions denoted in Fig. 1a. The fluxes are in units of 10^{-15} ergs $\text{cm}^{-2} \text{s}^{-1} \text{arcsec}^{-2}$, and the ratio is S to Si. r is scaled to that of the blast wave. The bump at $r \sim 0.45$ in the bottom right plot is due to a bright filamentary fragment as can be seen in region 3 of Fig. 1(a). The upper-left (outer) edge of this fragment is heated earlier and so shows S/Si line ratio profile resembling that of the whole section. The error bars show the 1σ uncertainties.

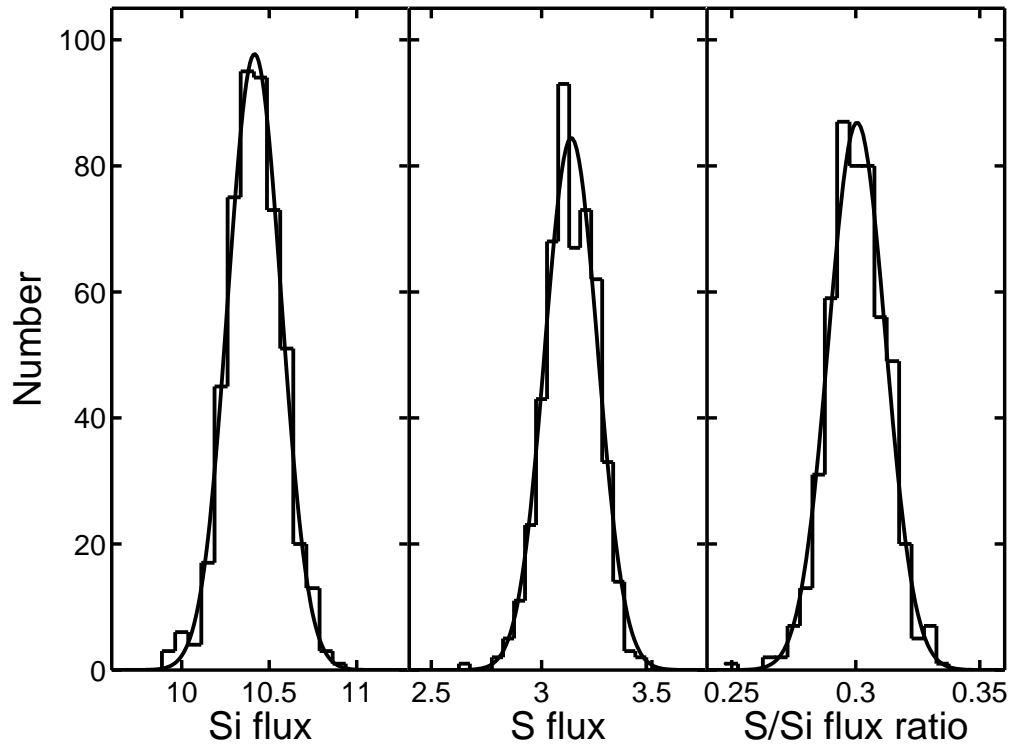


Fig. 4.— The distribution of the 500 simulated Si, S line fluxes and S/Si line flux ratios. It shows that the 1σ statistical errors of Si flux, S flux and S/Si flux ratio are about 1.5%, 3.7%, and 3.9%. The units of the fluxes are 10^{-15} ergs cm^{-2} s^{-1} .

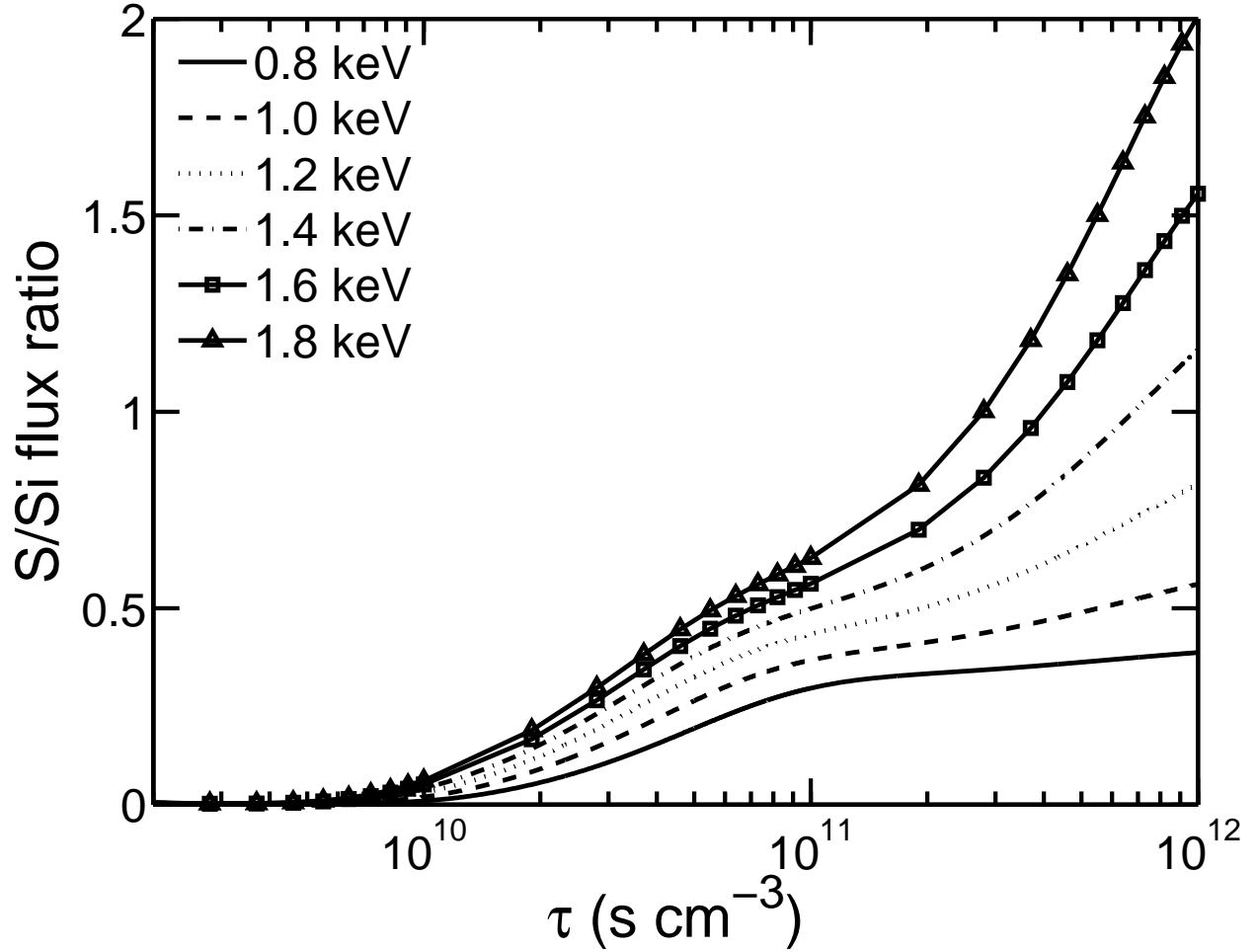


Fig. 5.— The relation between the He-like S to Si $K\alpha$ line ratio and ionization age τ for different plasma temperatures. The results are calculated with the VNEI model in XSPEC, and the S/Si abundance ratio is fixed at 1.35 times solar value as obtained by Hwang & Gotthelf (1997) for the Tycho’s SNR.

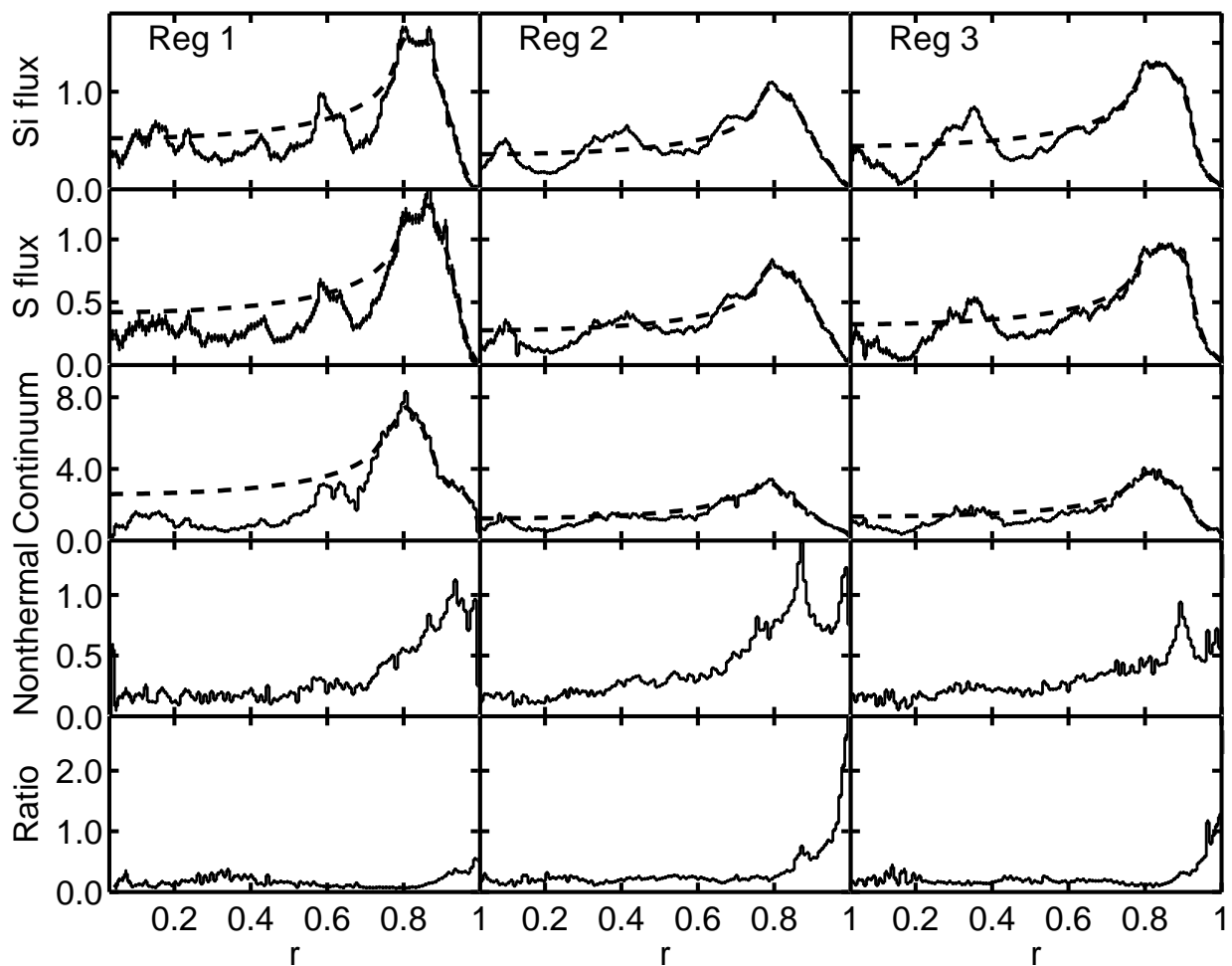


Fig. 6.— The measured radial surface flux distribution (solid lines) of the Si (top panel) line, the S (the 2nd panel) lines, the thermal continuum emission (0.85-1.5 keV plus 3.0-10.0 keV; the 3rd panel), the nonthermal emission (0.85-1.5 keV plus 3.0-10.0 keV; the 4th panel), the nonthermal to thermal continuum emission ratio (bottom panel), as well as the reprojected Si, S, and thermal continuum profiles (dashed lines). The fluxes are in units of 10^{-15} ergs cm^{-2} s^{-1} arcsec^{-2} , and the horizontal axis (r) has the same meaning as in Fig. 3.

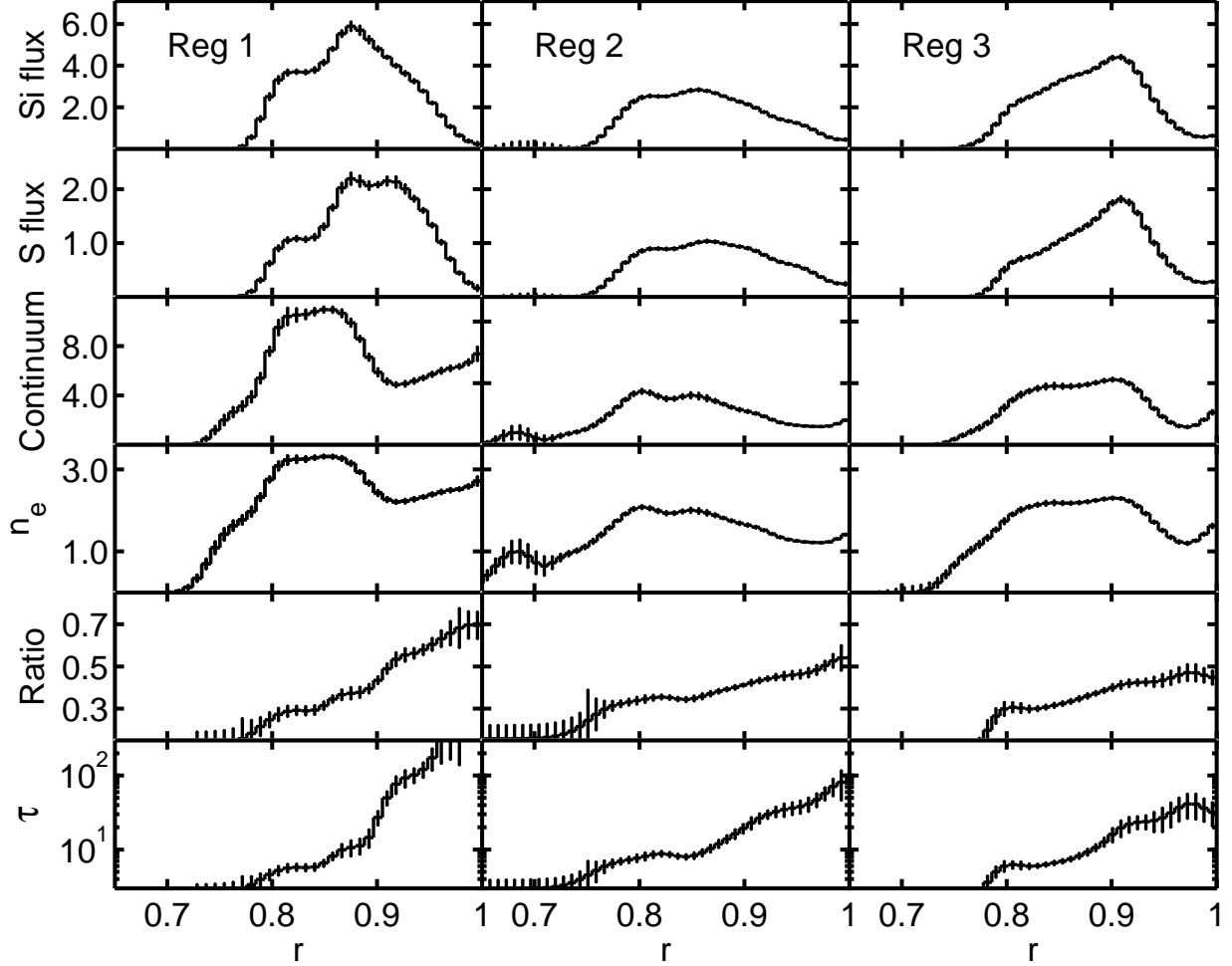


Fig. 7.— The radial profiles of the deprojected volume fluxes of the Si, S, and thermal continuum emission, as well as the scaled electron number density n_e , S/Si flux ratio, and the ionization age τ inferred from the line flux ratio assuming a constant temperature of 1.0 keV and S/Si abundance ratio of 1.35 times the solar value (Hwang & Gotthelf 1997). The fluxes are in units of 10^{-18} ergs $\text{cm}^{-2} \text{s}^{-1} \text{arcsec}^{-3}$. The continuum emission fluxes are for 0.85-1.5 keV plus 3.0-10.0 keV band with the nonthermal component subtracted, and the scaled electron number density n_e is simply a square root of the volume flux of the thermal continuum emission, because the flux is roughly proportional to n_e^2 as discussed in the text. The units of the scaled n_e are artificial, and units of τ are $10^{10} \text{ cm}^{-3} \text{ s}$. In the deprojection, a spherical symmetry is assumed. The error bars are obtained with a Monte-Carlo method as described in the text and Fig. 8. r has the same meaning as in Fig. 3.

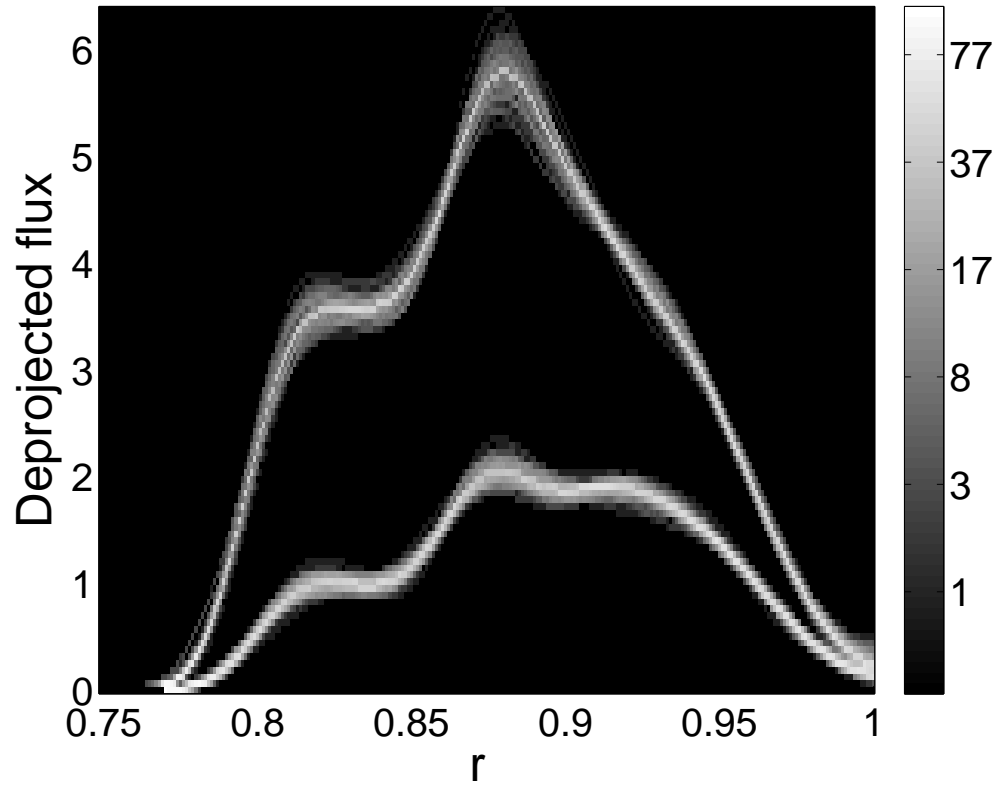


Fig. 8.— Distributions of the deprojected volume fluxes of the Si (the upper belt) and S (the lower belt) lines from the simulated surface brightness profiles for region 1 that defined in Fig. 1(a). The brightness of the belts represents the number of the simulated volume fluxes in the range defined by the vertical axis (in units of 10^{-18} ergs cm^{-2} s^{-1} arcsec^{-3}). r has the same meaning as in Fig. 3.